Geophysical Research Letters

RESEARCH LETTER
10.1029/2018GL080904

Key Points:
- We performed the dynamic source inversion of the 19 September (M_w7.1) 2017 intermediate-depth Mexican earthquake with a Particle Swarm Optimization algorithm
- The event was highly dissipative with a slow rupture propagation and scaling-consistent radiated energy
- The temperature rise associated with the specific fracture energy likely produced friction-induced melts in the fault core

Supporting Information:
- Supporting Information S1

Correspondence to:
V. M. Cruz-Atienza,
cruz@geofisica.unam.mx

Citation:
Mirwald, A., Cruz-Atienza, V. M., Díaz-Mojica, J., Iglesias, A., Singh, S. K., Villafuerte, C., & Tago, J. (2019).The 19 September 2017 (M_w7.1) intermediate-depth Mexican earthquake: A slow and energetically inefficient deadly shock. *Geophysical Research Letters*, *46*, 2054–2064. https://doi.org/10.1029/2018GL080904

Received 16 OCT 2018
Accepted 22 JAN 2019
Accepted article online 7 FEB 2019
Published online 26 FEB 2019

The 19 September 2017 (M_w7.1) Intermediate-Depth Mexican Earthquake: A Slow and Energetically Inefficient Deadly Shock

Aron Mirwald[1], Víctor M. Cruz-Atienza[1], John Díaz-Mojica[1], Arturo Iglesias[1], Shri K. Singh[1], Carlos Villafuerte[1], and Josué Tago[2]

[1]Instituto de Geofísica, Universidad Nacional Autónoma de México, Mexico City, Mexico, [2]Facultad de Ingeniería, Universidad Nacional Autónoma de México, Mexico City, Mexico

Abstract We investigate dynamic source parameters of the M_w7.1 Puebla-Morelos intermediate-depth earthquake ($h = 57$ km) of 19 September 2017, which devastated Mexico City. Our simple, elliptical source model, coupled with a new Particle Swarm Optimization algorithm, revealed rupture propagation within the subducted Cocos plate, featuring a high stress drop ($\Delta\tau = 14.9 \pm 5.6$ MPa) and a remarkably low radiation efficiency ($\eta_r = 0.16 \pm 0.09$). Fracture energy was large ($G = (1.04 \pm 0.3) \times 10^{16}$ J), producing a slow dissipative rupture ($V_r/V_s = 0.34 \pm 0.04$) with scaling-consistent radiated energy ($E_r = (1.8 \pm 0.9) \cdot 10^{15}$ J) and energy-moment ratio ($E_r/M_0 = 3.2 \times 10^{-5}$). About 84% of the available potential energy for the dynamic rupture was dissipated in the focal region, likely producing friction-induced melts in the fault core of 0.2–1.2 cm width due to heat production (700–1200 °C temperature rise). Such source features seem to be a universal signature of intermediate-depth earthquakes.

Plain Language Summary Devastation in central Mexico produced by the intermediate-depth (magnitude 7.1) Puebla-Morelos earthquake of 19 September 2017 has raised important questions about the seismic hazard in Mexico City, where more than 20 million people live. Probabilistic hazard in the city from intermediate-depth and shallower subduction events (i.e., as the 1985 quake that killed 15,000 people in the capital) is about the same despite that the first type of earthquakes is much less frequent. Understanding the source process of intermediate-depth earthquakes has been a major research topic since decades ago because they occur at depths where mechanical considerations for shallow earthquakes are no longer valid. Recent research has led to unexpected conclusions for this kind of events that were thought to be the consequence of fast and energetically efficient rupture processes. Through a novel technique, we investigate the Puebla-Morelos earthquake to better understand the generating physics of the strong ground motions. We show that the event was extraordinarily slow and inefficient and that this does not contradict the large ground accelerations. More than 84% of the earthquake energy was dissipated in the source region likely producing rock melting in the geological fault hosting the rupture process.

1. Introduction

On 19 September 2017, an M_w7.1 intermediate-depth normal-faulting earthquake (IDE) occurred in the subducting Cocos plate at 57-km depth, with epicentral distance of 114 km from Mexico City (Cruz-Atienza et al., 2017; Singh et al., 2018; Figure 1). The peak ground acceleration (PGA) at the rock reference site of Ciudad Universitaria was 57 cm/s^2, twice the value recorded at that site during the 1985 devastating earthquake (29 cm/s^2). The earthquake resulted in 369 deaths, of which more than two thirds perished in the capital, where 57 buildings suffered total or partial collapse. Devastation produced by an IDE in the country is not unusual. Several past intraslab earthquakes, as the great M_w8.2 rupture offshore the states of Oaxaca and Chiapas on 8 September 2017 (Okuwaki & Yagi, 2017; Suárez et al., 2019), have also caused large damage in other regions of Mexico (see; Singh et al., 2018, for a historical overview of IDEs in Mexico).

Despite the hazard that IDEs represent in Mexico and other regions of the globe, the physics of this kind of events has challenged the seismological community for decades (Frohlich, 2006). At focal depths below 30 km, brittle failure should be inhibited due to the high normal stresses and frictional stability (Green & Houston, 1995; Scholz, 1998). Yet most IDEs are characterized by unstable slip radiating high frequencies

(Frohlich, 2006). Dehydration reactions at those depths have often been invoked to explain brittle fracture (Hacker et al., 2003). Water release from mineralogical phase transitions could counteract the confining pressure directly (dehydration embrittlement; Jung et al., 2004) or indirectly (dehydration-driven stress transfer; Ferrand et al., 2017), enabling a brittle fracture.

However, it is also possible that brittle fracture is not responsible for IDEs. Thermal shear runaway in the focal region can generate highly localized ductile deformation and slip instabilities (Kanamori et al., 1998; Prieto et al., 2012). This mechanism was shown to be plausible by numerical simulations (Braeck & Podladchikov, 2007; John et al., 2009) and geological evidence (Andersen et al., 2008; Di Toro et al., 2005; John et al., 2009). Recently, local and global seismological studies have shown that most of IDEs have a low radiation efficiency, suggesting that thermal shear runaway is the leading source mechanism of IDEs (Díaz-Mojica et al., 2014; Nishitsuji & Mori, 2013; Prieto et al., 2013, 2017).

Advances in source imaging currently permit the retrieval of some dynamic rupture parameters directly from ground motion records. After the pioneering work of Peyrat and Olsen (2004), a few other efforts have led to improved methodologies for inverting the friction and stress changes on seismogenic faults (Díaz-Mojica et al., 2014; Di Carli et al., 2010; Herrera et al., 2017; Ruiz & Madariaga, 2013; Twardzik et al., 2014). Since these methods model the spontaneous rupture process to explain the observed seismograms (by solving the elastodynamic equations coupled with a fault-friction constitutive law), they allow assessment of fundamental properties of the source, such as the energy partition and its relation with the rupture kinematics.

In this work, we present the dynamic source inversion of the 2017 Puebla-Morelos earthquake to investigate the physics of the source process that originated the devastating ground motion in central Mexico. To this purpose, we improved the methodology introduced by Díaz-Mojica et al. (2014), by implementing a new Particle Swarm Optimization (PSO) algorithm (Eberhart & Kennedy, 1995) that takes advantage of parallel computing, high convergence rates and a thorough exploration of the model space around the best solutions.

2. Dynamic Source Inversion

2.1. Source Model

We model the earthquake rupture as a frictional process on a fault plane embedded in a 3-D elastic full space. Sliding begins when the shear traction in the nucleation zone (NZ) exceeds the static fault strength. In nature, the traction builds up gradually due to tectonic loading. Here, the shear traction in the NZ, which we assume as a 3-km radius circular patch, is prescribed slightly higher than the static strength of the fault so that the spontaneous rupture initiates with the simulation. To stop rupture propagation, we assume a barrier model that makes the strength of the rock infinite outside the source. The rupture area has an elliptical shape, which is a reasonable constraint for moderate-sized IDEs that generally show simpler and localized slip distributions (Díaz-Mojica et al., 2014; Di Carli et al., 2010; Ruiz & Madariaga, 2013).

We adopt the linear slip-weakening friction law (Ida, 1972) that depends on three constitutive parameters: the static (μ_s) and dynamic (μ_d) friction coefficients, and the slip-weakening distance (D_c). We assume a constant fault normal traction equal to the lithostatic pressure at 60-km depth (1,564 MPa), although this is irrelevant for the rupture process because seismic radiation only depends on the relative stress changes. We fix μ_d equal to 0.5 and invert for the change of friction coefficient from the static to the dynamic levels, $\Delta\mu$. We also invert for D_c, the last constitutive parameter defining our friction model.

The source model is determined by nine parameters: the initial shear tractions in the NZ and on the fault outside the NZ, the change of the friction coefficient, the slip-weakening distance, and the five geometrical parameters of the ellipse (lengths of its two semiaxes, two coordinates of its center with respect to the NZ, and its rotation angle). From models parameterized in this way, we can derive physical quantities involved in the rupture process (Díaz-Mojica et al., 2014) such as the fracture energy, G, the radiated energy, E_r, and, hence, the radiation efficiency, $\eta_r = E_r/(E_r + G)$, which tells how dissipative is the rupture process.

2.2. Inversion Method

The dynamic source inversion problem has been solved using heuristic strategies such as the neighborhood (e.g., Di Carli et al., 2010; Ruiz & Madariaga, 2013) and genetic (Díaz-Mojica et al., 2014) algorithms. In this work we introduce a new PSO algorithm to invert the rupture dynamics, which has the remarkable capacity to thoroughly sample the neighborhood of optimal solutions. Problem solving may be seen as a

Table 1
Inverted and Derived Parameters of Our Preferred Source Model

Symbol	Parameter	Range	Value
Inverted			
D_c	Slip-weakening distance	0.2–1 m	0.6 ± 0.3 m
$\Delta\mu$	Increment of friction coefficient	0.015–0.5	0.035 ± 0.007
$\Delta\tau$	Stress drop in fault	0–48 MPa	14.9 ± 5.6 MPa
$\Delta\tau^n$	Stress drop in NZ	18–78 MPa	55 ± 11 MPa
A	Area	80–1,250 km^2	713 ± 250 km^2
Derived			
G	Fracture energy	—	$(1.04 \pm 0.3) \cdot 10^{16}$ J
E_r	Radiated energy	—	$(1.8 \pm 0.9) \cdot 10^{15}$ J
η_r	Radiation efficiency	—	0.16 ± 0.09
κ	approximate ratio of strain energy to G_c	—	1.3 ± 0.2
V_r	Rupture velocity	—	$(0.34 \pm 0.04)V_s$

Note. Columns 3 and 4 provide the search range for the inverted parameters and the obtained mean values with their standard deviations for both the inverted and derived parameters, respectively. NZ = nucleation zone.

population-wide phenomenon, emerging from the behaviour of the individuals through their interactions. In any case, populations are organized according to some sort of communication structure, often thought of as a social network. In PSO a number of simple entities—the particles—are placed in the model space, and each evaluates the objective (or misfit) function at its current location. Each particle then determines its movement through the space by combining some aspect of the history of its own current and best locations with those of one or more members of the swarm, with some random perturbations. Eventually, the swarm as a whole, like a flock of birds collectively foraging for food, is likely to move close to an optimum of the objective function (Poli et al., 2007). The PSO has proven to be very efficient for a large class of multiparametric nonlinear problems (Blum & Li, 2008). Our PSO algorithm follows Suganthan (1999) with an increasing size of the models' vicinity to prevent premature convergence. Its parameters, listed in supporting information Table S1, were chosen based on a parametric study we performed for the nine-dimensional Langerman function (Jamil & Yang, 2013). The size of the population we used was 420 particles (i.e., models), and we ran the inversions for 50 generations, resulting in $420 \times 50 = 21{,}000$ dynamic-source-tested models per inversion. Since we performed 12 inversions per auxiliary fault plane as explained later in section 3, we explored a total of 504,000 dynamic source models to generate our preferred solution. In Table 1 we provide the searching ranges of the model space. To avoid wasting computational time when solving unfeasible models, we constrained the parameters in such way that the initial traction was always larger than the static strength in the NZ, and lower than that in the rest of the fault.

To quantify the quality of the source models, we use a misfit function that involves the cross correlation between observed and synthetic seismograms (Díaz-Mojica et al., 2014):

$$f = \frac{1}{6N} \sum \left(\frac{\tau_{\max} - \tau_c}{2\tau_c} - \frac{\mathtt{cross}(x_{\text{obs}} - x_{\text{syn}})}{\mathtt{auto}(x_{\text{obs}}) + \mathtt{auto}(x_{\text{syn}})} \right), \tag{1}$$

where the sum is over the three components for all (N) seismic stations. The first term on the right-hand side accounts for the time shift between the signals that depends on the characteristic time, τ_c, which is approximately equal to the source duration halftime (in this case $\tau_c = 7s$; Díaz-Mojica et al., 2014), and $\tau_{\max}$ is the absolute value of the time shift for the maximum cross-correlation coefficient. The second term involves the maximum of the cross-correlation and autocorrelation functions and accounts for the similarity of waveform and amplitude.

Following Di Carli et al. (2010), the forward problem is solved in two steps. First, the dynamic rupture is simulated using a highly accurate 3-D traction-at-slip-node finite-difference method (Dalguer & Day, 2007) as compared with most of the well-established numerical methods (Harris et al., 2018), in a cubic domain

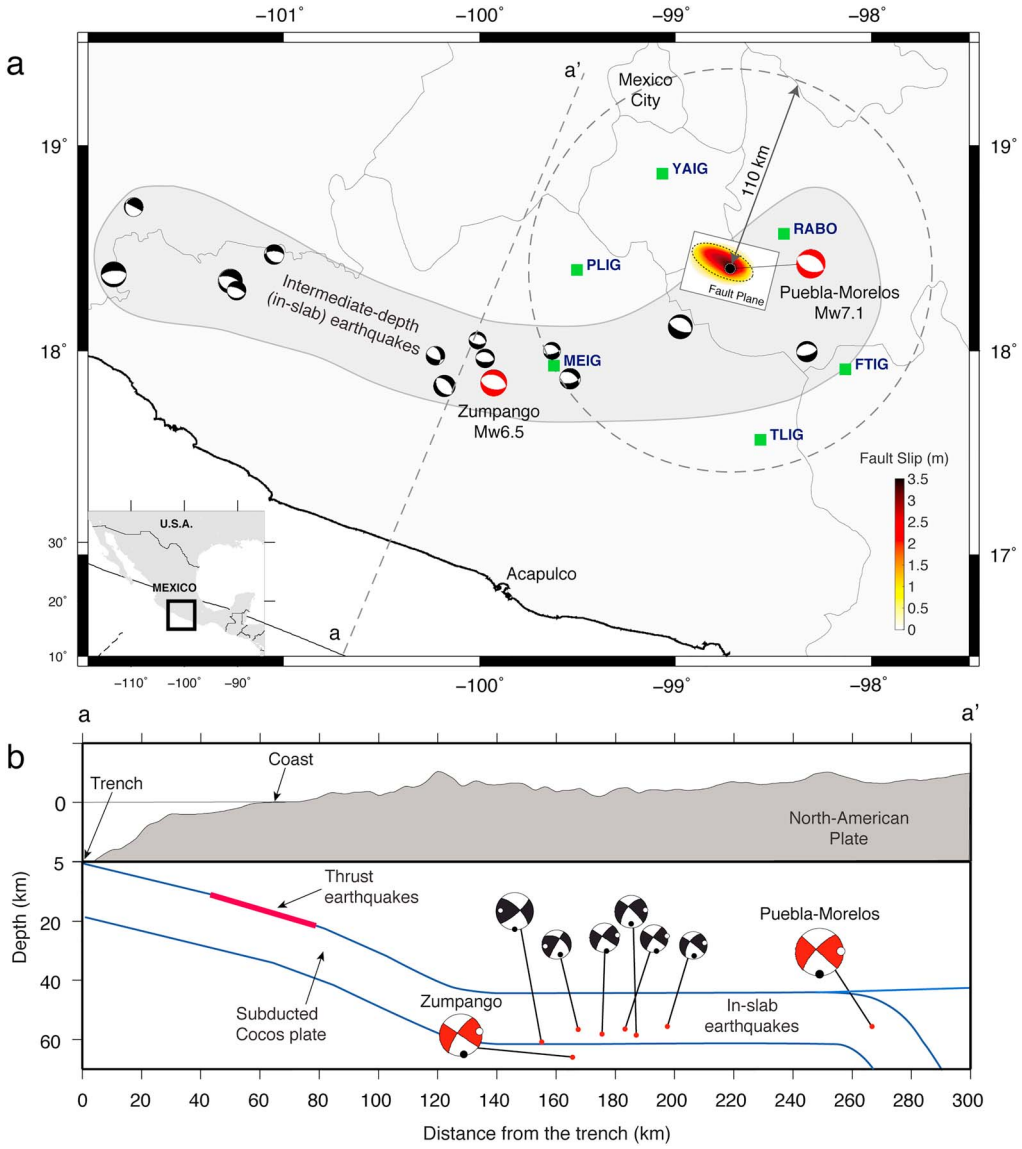

Figure 1. Map showing significant IDEs in central Mexico. (a) Location of strong motion stations (green squares) used for the inversion of the Puebla-Morelos event (modified from; Cruz-Atienza et al., 2017). The straight dashed line depicts the cross section shown below. (b) Cross section showing the tectonic setting of the region and the projection of some IDEs. IDE = intermediate-depth earthquake.

with 50-km length per side and a grid size of 400 m. We verified that such grid size virtually produces the same solutions as for 300 m in a wide range of constitutive parameters including those explored in our inversions (e.g., rupture time errors smaller than 10% in all cases). The time step was adjusted according to the stability criterion. The cube contains the fault plane where the friction law is imposed. Around the cube, the outgoing seismic energy is absorbed with a Perfectly Matched Layer (Marcinkovich & Olsen, 2003) to simulate an infinite space. Second, the output source kinematics is used to propagate the wavefield up to the stations by convolving the slip rate functions with the double-couple Green's functions computed using a discrete wavenumber method (Bouchon, 1981) in a layered medium appropriate for the region (Campillo et al., 1996). The dynamic source inversion methods are very time consuming. In our case, each forward problem took about 15 min in a single 2.4-GHz Intel Xeon processor. Each inversion was run in parallel with the PSO algorithm over 210 processors. Considering a population of 420 models and 50 generations, each inversion lasted about 25 hrs.

2.3. Data and Focal Mechanism

We used accelerograms of six strong motion stations belonging to the National University of Mexico (UNAM) with an epicentral distance smaller than 110 km (Figure 1a). We selected the stations avoiding those with large site effects, while maintaining a good azimuthal coverage. The seismograms were aligned with the theoretical *P* wave arrival times predicted by the regional velocity model (Campillo et al., 1996). Then, the accelerograms were band-pass filtered between 0.05 and 0.15 Hz and integrated twice to obtain the displacements that were inverted. The inverted frequency band contains the corner frequency of the event, f_c ~0.08 Hz (supporting information Figure S1; consistent with the source duration of ~13 s reported by the U.S. Geological Survey), and thus essential information of the source finiteness. We choose the upper cutoff frequency to avoid unmodeled effects due to the simplicity of both the source model and the 1-D velocity structure, which prevent us to solve for source details that are not critical for capturing the overall physics of the rupture process.

For an ω^2 Brune source model, the radiated energy contained in frequencies $f < 2 * f_c$ (i.e., below 0.16 Hz in this case) is less than 42% of the total (Singh & Ordaz, 1994). However, since low frequencies are intrinsically linked to high frequencies through the downscale causal relationship given by the elastodynamic and fault constitutive equations governing the propagating crack, the source energy partition is reasonably well solved provided that the fault mechanical model we assumed is a good proxy. This has been proven to be so by Díaz-Mojica et al. (2014) and can be seen in supporting information Figure S1 for this event, where the spectrum of our preferred source model above 0.16 Hz is consistent with two other functions determined independently and slightly above the ω^2 Brune's prediction.

Since it was not possible to determine unambiguously the fault plane using the small aftershocks sequence, we inverted the source process for both auxiliary planes (Figure 1). The inversions yielded similar model parameters for both planes, so we decided to discuss only the results for the fault dipping to the south ($\phi = 108°, \delta = 47°, \lambda = -98°$), which yielded 20% better fits with the observed waveforms.

3. Results

Because of the stochastic nature of the optimization method, we decided to run multiple inversions in the same model space. Although the best misfit values from all inversions were of the same order, we noticed that the associated parameters were different to some extent and that they were interdependent. As expected, (a) larger stress drops were generally associated with smaller rupture areas and larger D_c, and (b) lower rupture velocities were often associated with larger D_c. Ruiz and Madariaga (2013) noticed similar trade-offs between these parameters in their dynamic source inversions. However, the variation range of the preferred models from our inversions is relatively small. More importantly, there are quasi-invariant metaparameters across the solutions such as the radiated energy, fracture energy, radiation efficiency, and rupture velocity. This means that all models essentially share the same energy partition and rupture kinematics.

Our solution models correspond to the best fit individuals from 12 independent inversions, whose misfit values are smaller than 0.15. We took as the final, preferred solution (Table 1) the average of these models along with their standard deviation per parameter. The seismogram fits are shown in Figure 2, where we compare the observed waveforms (black curves) with the average waveforms from the selected models (red curves) along with the associated standard deviations (pink band). Despite the simplicity of the source model and the velocity structure, most of the waveforms and amplitudes are well reproduced in the three components, which gives us confidence to our solution models.

In Figure 3a we show the average final slip distributions from the 12 selected models and the geometry of the best fit solution whose misfit value is 0.11 (white dashed ellipse). Rupture predominantly propagates to the northwest and updip with an average final slip of 2.1 ± 0.3 m, which is a reasonable value for earthquakes of this size. If we project the rupture path from the NZ to the left extremity of the rupture into the Earth's surface, rupture directivity points roughly toward Mexico City (Figure 1a), suggesting that the anomalously high ground accelerations and velocities observed in that direction could be due to source directivity (Singh et al., 2018). It is worth mentioning that a consistent direction of rupture directivity was found for all solutions obtained from the inversions done for the other auxiliary fault plane, dipping to the north (not shown).

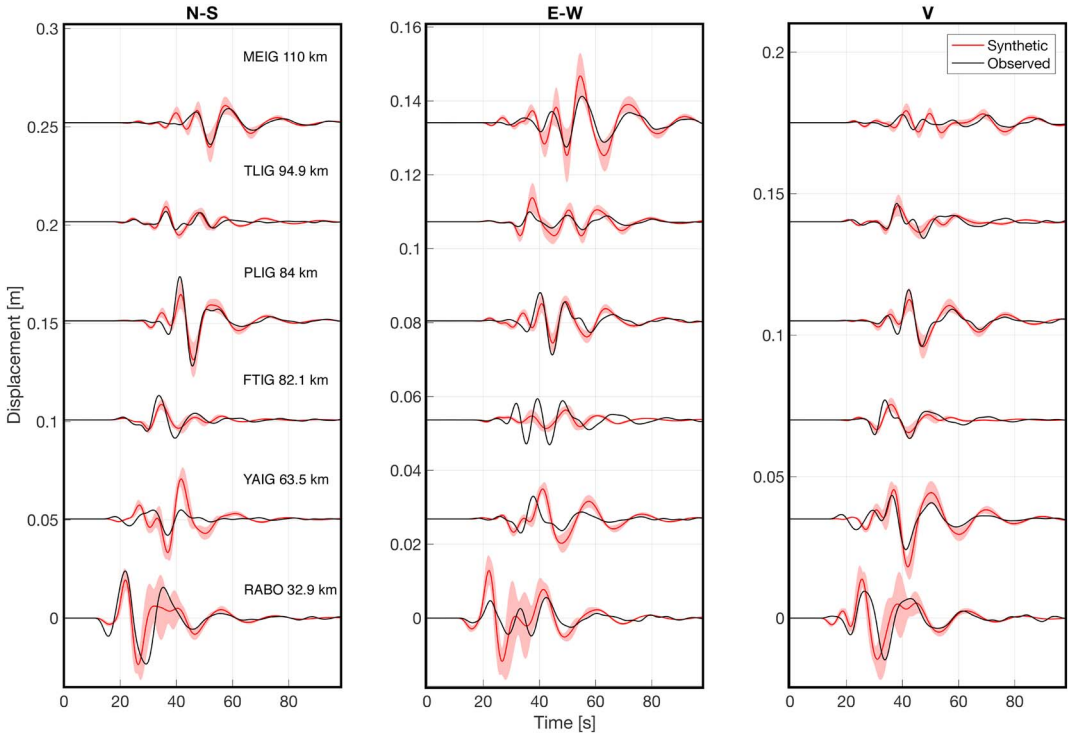

Figure 2. Observed (black) and synthetic (red) seismograms in the frequency band 0.05–0.15 Hz. The black lines are the average of the 12 solution models from independent inversions, and the shaded pink areas depict 2 times the associated standard deviation.

Although rupture velocity is remarkably low across large parts of the fault (average speed of 0.34 ± 0.04 of the shear wave speed; Table 1), it is also highly variable (Figure 3b). Just after nucleation, rupture propagates with speed around 0.5*Vs* along ~10-km updip from the NZ and then slows down rapidly, specially along strike, where it almost stops a few kilometers to the northwest (i.e., with speeds of 0.1–0.2 *Vs*). Rupture finally accelerates around 20 km from the NZ to reach again values around 0.5*Vs* close to the northwest fault extremity. We notice that the relatively high front velocity just after nucleation may be an artifact of the highly stressed NZ required to sustain the rupture process in the whole fault.

Dynamic crack theory predicts that the faster the rupture front, the larger is the radiation efficiency. This is shown in Figure 4a for the three different fracture modes (gray lines). Since fracture energy for a given model is almost constant across the fault because of the slip-weakening friction law (i.e., it is constant except in a narrow belt next to the fault edge where the final slip is smaller than D_c), rupture speed variations should map bulk regions where radiation of seismic energy (or the seismic moment rate) is enhanced. Figure 3c confirms such expectation by revealing two maxima of the peak slip rate that spatially correlate with fault regions where V_r is maximum (compare with panel b). Accordingly, the average moment rate function (black line in Figure 3d) shows the associated bumps centered at 1 and 9 s, as well as a total source duration close to 16 s. Although the stress drop in the nucleation zone has been inverted, we notice that the timing and width of the first peak could be biased to some extent by the initial kick imposed to initiate rupture. However, as seen in Figures 3b and 3d, such effect should not be preponderant in the relatively long (~13 s long) rupture history after the first 2–3 s of rupture propagation.

Our preferred model exhibits a stress drop of 14.9 ± 5.6 MPa, which is high compared with typical values for shallow earthquakes, but consistent with IDEs in Mexico (García et al., 2004) and at global scale, which have a mean value around 15 MPa (Prieto et al., 2012; Poli & Prieto, 2016). From the model parameters, we derived the radiated energy $E_r = (1.8 \pm 0.9) \cdot 10^{15}$ J, the fracture energy $G = (1.04 \pm 0.3) \cdot 10^{16}$ J and a remarkably low radiation efficiency $\eta_r = 0.16 \pm 0.09$. All the inverted and derived parameters from our preferred model are reported in Table 1.

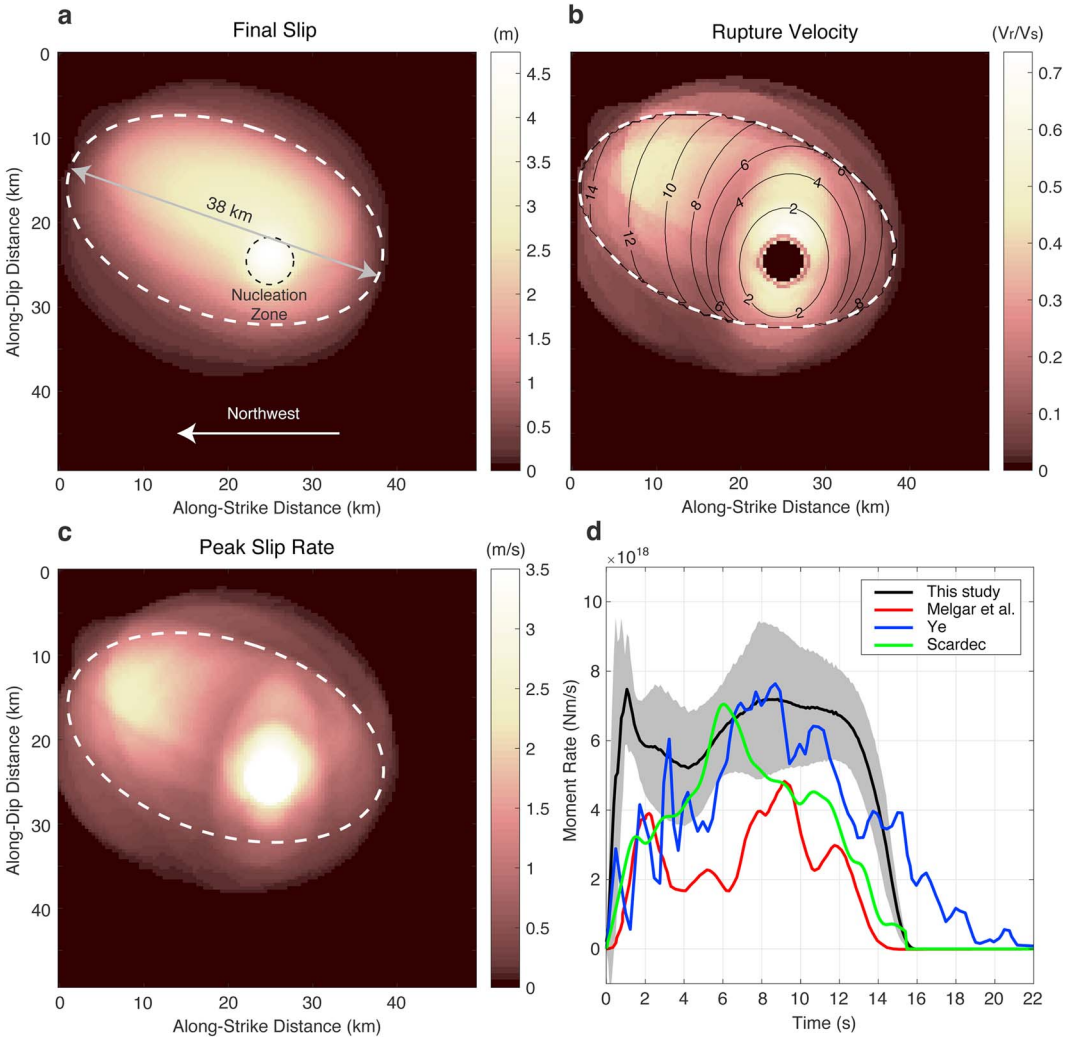

Figure 3. Averages of the 12 solution models where the dashed ellipse corresponds to the best fit model geometry. (a) Final slip, (b) rupture velocity normalized by a shear wave speed of 4.7 km/s along with the rupture time contours (in seconds) of the best fit model, (c) peak slip rate, and (d) moment rate function along with the standard deviation in gray. All models share the same nucleation zone geometry (black dashed circle).

4. Discussion

Similar to the analysis of the 2011 Zumpango IDE (M_w6.5) in Guerrero, Mexico (Díaz-Mojica et al., 2014), the inversion of the Puebla-Morelos event revealed that the average rupture speed ($Vr/Vs \sim 0.34$) and the radiation efficiency (η_r ~0.16) were also remarkably low (Figure 4a). As expected for intraslab Mexican earthquakes, the stress drop ($\Delta\tau$ ~15 MPa) was relatively high. Similar results for IDEs have been reported in the Japan subduction zone (Nishitsuji & Mori, 2013), and more recently at a global scale (Poli & Prieto, 2016) and below the Wyoming Craton, USA, in a completely different tectonic setting (Prieto et al., 2017), suggesting that slow, inefficient processes characterize the source of IDEs.

Although such rupture properties are typical of tsunami earthquakes (see Figure 4a), the 2017 M_w7.1 shock produced a Fourier acceleration spectrum at Ciudad Universitaria between 1 and 2 s 2 times larger than observed for previous Mexican IDEs with similar magnitude reduced to the same hypocentral distance (Singh et al., 2018). This shows that despite the highly dissipative source process and the slow rupture propagation, the event generated high radiation of relatively short period waves. This is opposite to tsunami earthquakes, which are characterized by large M_S-M_w disparities and anomalously low values of the ratio E_r/M_0 (Ammon et al., 2006; Newman & Okal, 1998). In the case of the Puebla-Morelos IDE, our inversion yielded $E_r/M_0 = 3.2 \times 10^{-}5$, which is consistent with the value found from the dynamic source inversion

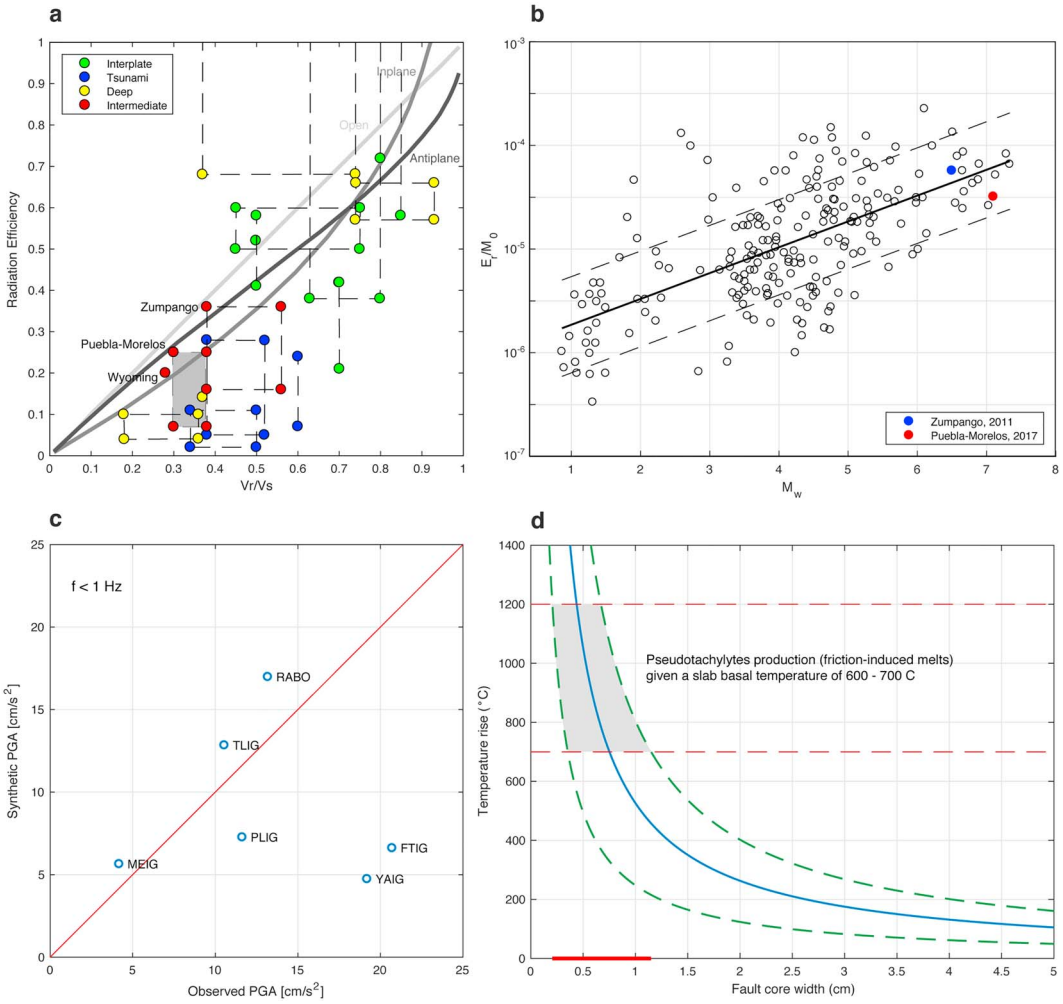

Figure 4. (a) Radiation efficiency (η_r) as a function of rupture velocity (V_r) normalized by the shear wave speed (V_s) for different types of earthquakes including the Puebla-Morelos and Zumpango events in central Mexico. Reported IDEs (red dots) share the same properties as tsunami earthquakes, with very low rupture velocity and radiation efficiency. Gray lines depict theoretical predictions for the three different fracture modes (modified from; Kanamori & Brodsky, 2004). (b) Energy-moment ratios for global earthquakes as a function of magnitude M_w taken from Kanamori and Brodsky (2004) along with values found for the Puebla-Morelos and Zumpango IDEs. The straight lines depict the best linear fit (solid) and the 60th percentile (dashed). (c) Horizontal components geometric mean of the observed and synthetic (best fit model) peak ground accelerations below 1 Hz. (d) Temperature rise as a function of the fault core width according to equation (2). The green dashed lines depict the temperature range associated to our fracture energy uncertainty, and the red dashed lines the range where peridotites and gabbroic rocks melt at the earthquake depth. IDE = intermediate-depth earthquake.

of the M_w6.5 Zumpango IDE in the region (Díaz-Mojica et al., 2014), and with those of many earthquakes at a global scale (Figure 4b).

Careful examination of the waveforms does not reveal a preponderant source directivity as clearly seen for a similar IDE in the region (Singh et al., 2014). As a matter of fact, in the absence of strong directivity such as in our preferred source model, strong motions below 1 Hz can be satisfactorily explained with the dynamic rupture properties described in the last section. The peak focal-particle acceleration in the two patches with maximum slip rates (Figure 3c) are significantly higher than 0.5g (i.e., between 415 and 585 cm/s^2). These values in the source region are consistent with most of the PGAs observed at the stations including RABO, the closest site (hypocentral distance of 65 km), for periods longer than 1 s as shown in Figure 4c. Model underestimations in the strike-parallel direction (i.e., at stations YAIG and FTIG) are certainly due to the source model simplicity, specially at FTIG toward the southeast, where even kinematic source inversions poorly fit the waveforms (Melgar et al., 2018). Two main features of our moment rate function are consistent

with previous estimates (Figure 3d): the duration of about 16 s and two peaks in the moment release (between 1 and 4 s, and between 5 and 12 s). Although the source time functions are remarkably different among each other in the timing of the main peaks, they share similar amplitudes except for the solution reported by Melgar et al. (2018), which significantly underestimates the scalar moment. Integration of the moment rate functions gives scalar moments of 1.05^{20} Nm ($M_w = 7.28$), 3.5^{19} Nm ($M_w = 6.96$), 7.63^{19} Nm ($M_w = 7.18$), and 5.8^{19} Nm ($M_w = 7.11$), for our preferred model, and the solutions from Melgar et al. (2018), Ye (2018), and Vallée and Duet (2016), respectively.

Most interplate earthquakes have radiation efficiencies larger than 0.5 (Venkataraman & Kanamori, 2004; Figure 4a), which implies $G < E_r$. Since $\eta_r \sim 0.16$ for the Puebla-Morelos event, then $G = 5.3E_r$ in this case. This means that ~84% of the available potential energy for the dynamic process of faulting was dissipated in the focal region. Energy dissipation during an earthquake may involve different processes such as off-fault fracturing, plastic deformation, or heat production. Among them, heat production is certainly a preponderant dissipative mechanism that may translate into pseudotachylytes generation (friction-induced melts) in the fault core (Di Toro et al., 2005; Kanamori et al., 1998). Since most of the mechanical energy during rupture is converted into work against frictional stresses, it has been shown that about 90% of the energy partition goes into heat production for most large earthquakes (Cocco et al., 2006). Could fault core melting have happened during the Puebla-Morelos event? At the tip of the rupture front (i.e., in the stress breakdown zone), the temperature rise, ΔT, is related to the specific fracture energy, G_c (or breakdown work density, namely, $W_b = G/A$), as (Prieto et al., 2013)

$$\Delta T = \frac{G_c}{C\rho w}, \tag{2}$$

where $C \sim 1$ J·g^{-1}·°C^{-1} is the heat capacity, ρ ~3230 kg/m^3, and w is the fault core width. This equation assumes that the whole fracture energy is dissipated into heat. In our model, G_c is equal to $(1.7 \pm 0.9) \cdot 10^7$ J/m^2 in average. Figure 4d shows the temperature rise for different widths predicted by equation (2). According to thermal models of the subducted Cocos plate, the temperature of the slab where the earthquake took place is between 600 and 700 °C (Manea & Manea, 2011; Perry et al., 2016). The melting temperature of peridotite and gabbroic rocks at those depths (i.e., at 1.5–2 GPa) range between 1400 and 1800 °C (Katz et al., 2003; Nielsen et al., 2010; Philpotts & Ague, 2009; Takahashi & Scarfe, 1985). Therefore, we expect melting to occur at fault core widths between 0.2 and 1.2 cm (see red line in Figure 4d). Field observations show that exhumed fault core widths are variable, but most fault veins and pseudotachylites related to subduction earthquakes are between 0.1 and 3 cm (Andersen & Austrheim, 2006; Obata & Karato, 1995). Therefore, the temperature rise at the rupture front (estimated between 700 and 1200 °C) may indeed have resulted in rock melting as suggested for other IDEs (Prieto et al., 2013). Note that we did not consider the heat generated by the total slip involving the dynamic friction level in large parts of the fault, as done by Kanamori et al. (1998), that would yield to a higher temperature rise.

Our heat production estimates suggest that melting may have happened at the rupture tip of the Puebla-Morelos earthquake (absolute temperatures at the tip of 1300–1900 °C), supporting the idea that a thermal runaway process could be a preponderant mechanism enhancing unstable slip through lubrication effects despite the high confining pressures of the focal region. Dehydration from water-rich minerals could also have played a role in the source region, which does not preclude the existence of the thermal runaway process (John et al., 2009).

5. Conclusions

We performed the dynamic source inversion of the 2017 intermediate-depth Puebla-Morelos earthquake with a new PSO algorithm. Our results indicate that the rupture was highly dissipative and remarkably slow. More than 84% of the available potential energy for the dynamic rupture propagation dissipated in the focal region. Considering the preexistent slab temperature and heat production during the rupture process, creation of pseudotachylytes (friction-induced melts) in the fault core is a plausible process that could enhance the slip instability by lubricating the fault core. Despite the large energy dissipation and the slow rupture propagation, our dynamic model explains most of the observed PGAs below 1 Hz (i.e., the excitation of relatively short period waves), which were responsible for the extreme ground motion observed in Mexico City. Independent estimates of IDEs energy balances in Guerrero and different tectonic settings across the globe

suggest that slow, inefficient ruptures with scaling-consistent energy radiation may by a universal feature of most earthquakes at intermediate depths.

Acknowledgments
This work was supported by the CONACyT grant 2017-01-6471, the UNAM-PAPIIT grant IG100617, the Japan-Mexico SATREPS project funded by JST/JICA/UNAM/CONACyT, and the graduate school scholarships program of CONACyT. We thank the "Servicio Sismológico Nacional" and the "Instituto de Ingeniría," both belonging to the "Universidad Nacional Autónoma de México" (UNAM), for the acceleration records used in this work. Seismic records can be obtained upon request to these institutions through the websites (http://www.ssn.unam.mx/contacto/ and http://aplicaciones.iingen.unam.mx/acelerogramasrsm/redacelerografica.aspx).

References

Ammon, C. J., Kanamori, H., Lay, T., & Velasco, A. A. (2006). The 17 July 2006 Java tsunami earthquake. *Geophysical Research Letters*, *33*, L234308. https://doi.org/10.1029/2006GL028005

Andersen, T. B., & Austrheim, H. (2006). Fossil earthquakes recorded by pseudotachylytes in mantle peridotite from the alpine subduction complex of Corsica. *Earth and Planetary Science Letters*, *242*, 58–72.

Andersen, T. B., Mair, K., Austrheim, H., Podladchikov, Y. Y., & Vrijmoed, J. C. (2008). Stress release in exhumed intermediate and deep earthquakes determined from ultramafic pseudotachylyte. *Geology*, *36*(12), 995–998.

Blum, C., & Li, X. (2008). Swarm intelligence in optimization. In C. Blum, & D. Merkle (Eds.), *Swarm intelligence*, *Natural computing series* (pp. 43–85). Heidelberg: Springer.

Bouchon, M. (1981). A simple method to calculate green's functions for elastic layered media. *Bulletin of the Seismological Society of America*, *71*(4), 959–971.

Braeck, S, & Podladchikov, Y. (2007). Spontaneous thermal runaway as an ultimate failure mechanism of materials. *Physical Review Letters*, *98*(9), 95504.

Campillo, M, Singh, S., Shapiro, N, Pacheco, J, & Hermann, R. (1996). Crustal structure south of the Mexican volcanic belt, based on group velocity dispersion. *Geofisica Internacional*, *35*(4), 361–370.

Cocco, M., Spudich, P., & Tinti, E. (2006). On the mechanical work absorbed on faults during earthquake ruptures. In R. Abercrombie, A. McGarr, G. Di Toro, & H. Kanamori (Eds.), *Radiated energy and the physics of earthquakes faulting, Geophysical Monograph Series* (Vol. 170, pp. 237–254). Washington, DC: American Geophysical Union. https://doi.org/10.1029/GM170

Cruz-Atienza, V. M., Singh, S. K., & Ordaz, M. (2017). ¿Qué ocurrió el 19 de septiembre de 2017 en México? Revista Digital Universitaria (RDU) (Vol. *18*, 7). https://doi.org/10.22201/codeic.16076079e.2017.v18n7.a10

Dalguer, L. A., & Day, S. M. (2007). Staggered-grid split-node method for spontaneous rupture simulation. *Journal of Geophysical Research*, *112*, B02302. https://doi.org/10.1029/2006JB004467

Di Carli, S., François-Holden, C., Peyrat, S., & Madariaga, R. (2010). Dynamic inversion of the 2000 Tottori earthquake based on elliptical subfault approximations. *Journal of Geophysical Research*, *115*, B12328. https://doi.org/10.1029/2009JB006358

Di Toro, G., Nielsen, S., & Pennacchioni, G. (2005). Earthquake rupture dynamics frozen in exhumed ancient faults. *Nature*, *436*(7053), 1009.

Díaz-Mojica, J., Cruz-Atienza, V. M., Madariaga, R., Singh, S. K., Tago, J., & Iglesias, A. (2014). Dynamic source inversion of the M6. 5 intermediate-depth Zumpango earthquake in central Mexico: A parallel genetic algorithm. *Journal of Geophysical Research: Solid Earth*, *119*, 7768–7785. https://doi.org/10.1002/2013JB010854

Eberhart, R., & Kennedy, J. (1995). A new optimizer using particle swarm theory. In *proceedings of the sixth international symposium on IEEE, Micro machine and human science, 1995. mhs'95*, pp. 39–43.

Ferrand, T. P., Hilairet, N., Incel, S., Deldicque, D., Labrousse, L., Gasc, J., et al. (2017). Dehydration-driven stress transfer triggers intermediate-depth earthquakes. *Nature communications*, *8*, 15247.

Frohlich, C. (2006). *Deep earthquakes*. Cambridge: Cambridge University Press.

García, D., Singh, S. K., Herráiz, M., Pacheco, J. F., & Ordaz, M. (2004). Inslab earthquakes of central Mexico: Q, source spectra, and stress drop. *Bulletin of the Seismological Society of America*, *94*(3), 789–802.

Green, H. W., & Houston, H. (1995). The mechanics of deep earthquakes. *Annual Review of Earth and Planetary Sciences*, *23*(1), 169–213.

Hacker, B. R., Peacock, S. M., Abers, G. A., & Holloway, S. D. (2003). Subduction factory: 2. Are intermediate-depth earthquakes in subducting slabs linked to metamorphic dehydration reactions? *Journal of Geophysical Research*, *108*(B1), 2030. https://doi.org/10.1029/2001JB001129

Harris, R., Barall, M., Aagaard, B., Ma, S., Roten, D., Olsen, K., et al. (2018). A suite of exercises for verifying dynamic earthquake rupture codes. *Seismological Research Letters*, *89*, 1146–1162.

Herrera, C., Ruiz, S., Madariaga, R., & Poli, P. (2017). Dynamic inversion of the 2015 Jujuy earthquake and similarity with other intraslab events. *Geophysical Journal International*, *209*(2), 866–875.

Ida, Y. (1972). Cohesive force across the tip of a longitudinal-shear crack and Griffith's specific surface energy. *Journal of Geophysical Research*, *77*(20), 3796–3805.

Jamil, M., & Yang, X.-S. (2013). A literature survey of benchmark functions for global optimization problems. *International Journal of Mathematical Modelling and Numerical Optimisation*, *4*, 150–194.

John, T., Medvedev, S., Rüpke, L. H., Andersen, T. B., Podladchikov, Y. Y., & Austrheim, H. (2009). Generation of intermediate-depth earthquakes by self-localizing thermal runaway. *Nature Geoscience*, *2*(2), 137.

Jung, H., Green Ii, H. W., & Dobrzhinetskaya, L. F. (2004). Intermediate-depth earthquake faulting by dehydration embrittlement with negative volume change. *Nature*, *428*(6982), 545.

Kanamori, H., Anderson, D. L., & Heaton, T. H. (1998). Frictional melting during the rupture of the 1994 Bolivian earthquake. *Science*, *279*(5352), 839–842.

Kanamori, H., & Brodsky, E. E. (2004). The physics of earthquakes. *Reports on Progress in Physics*, *67*(8), 1429.

Katz, R. F., Spiegelman, M., & Langmuir, C. H. (2003). A new parameterization of hydrous mantle melting. *Geochemistry, Geophysics, Geosystems*, *4*(9), 1073. https://doi.org/10.1029/2002GC000433

Manea, V. C., & Manea, M. (2011). Flat-slab thermal structure and evolution beneath central Mexico. *Pure and Applied Geophysics*, *168*(8-9), 1475–1487.

Marcinkovich, C., & Olsen, K. (2003). On the implementation of perfectly matched layers in a three-dimensional fourth-order velocity-stress finite difference scheme. *Journal of Geophysical Research*, *108*(B5), 2276. https://doi.org/10.1029/2002JB002235

Melgar, D., Pérez-Campos, X., Ramirez-Guzman, L., Spica, Z., Espíndola, V. H., Hammond, W. C., & Cabral-Cano, E. (2018). Bend faulting at the edge of a flat slab: The 2017 M_w7. 1 Puebla-Morelos, Mexico earthquake. *Geophysical Research Letters*, *45*, 2633–2641. https://doi.org/10.1002/2017GL076895

Newman, A. V., & Okal, E. A. (1998). Teleseismic estimates of radiated seismic energy: The E/M 0 discriminant for tsunami earthquakes. *Journal of Geophysical Research*, *103*(B11), 26885–26898.

Nielsen, S., Mosca, P., Giberti, G., Di Toro, G., Hirose, T., & Shimamoto, T. (2010). On the transient behavior of frictional melt during seismic slip. *Journal of Geophysical Research*, *115*, B10301. https://doi.org/10.1029/2009JB007020

Nishitsuji, Y., & Mori, J. (2013). Source parameters and radiation efficiency for intermediate-depth earthquakes in northeast Japan. *Geophysical Journal International*, *196*(2), 1247–1259.

Obata, M., & Karato, S.-i. (1995). Ultramafic pseudotachylite from the Balmuccia peridotite, Ivrea-Verbano Zone, northern Italy. *Tectonophysics*, *242*, 313–328.

Okuwaki, R., & Yagi, Y. (2017). Rupture process during the M_w 8.1 2017 Chiapas Mexico earthquake: Shallow intraplate normal faulting by slab bending. *Geophysical Research Letters*, *44*, 11,816–11,823. https://doi.org/10.1002/2017GL075956

Perry, M., Spinelli, G. A., Wada, I., & He, J. (2016). Modeled temperatures and fluid source distributions for the Mexican subduction zone: Effects of hydrothermal circulation and implications for plate boundary seismic processes. *Geochemistry, Geophysics, Geosystems*, *17*, 550–570. https://doi.org/10.1002/2015GC006148

Peyrat, S, & Olsen, K. (2004). Nonlinear dynamic rupture inversion of the 2000 western Tottori, Japan, earthquake. *Geophysical research letters*, *31*, L05604. https://doi.org/10.1029/2003GL019058

Philpotts, A., & Ague, J. (2009). *Principles of igneous and metamorphic petrology* (2nd ed.). Cambridge : Cambridge University Press.

Poli, R., Kennedy, J., & Blackwell, T. (2007). Particle swarm optimization. An overview, Swarm Intell.

Poli, P., & Prieto, G. A. (2016). Global rupture parameters for deep and intermediate-depth earthquakes. *Journal of Geophysical Research: Solid Earth*, *121*, 8871–8887. https://doi.org/10.1002/2016JB013521

Prieto, G. A., Beroza, G. C., Barrett, S. A., López, G. A., & Florez, M. (2012). Earthquake nests as natural laboratories for the study of intermediate-depth earthquake mechanics. *Tectonophysics*, *570*, 42–56.

Prieto, G. A., Florez, M., Barrett, S. A., Beroza, G. C., Pedraza, P., Blanco, J. F., & Poveda, E. (2013). Seismic evidence for thermal runaway during intermediate-depth earthquake rupture. *Geophysical Research Letters*, *40*, 6064–6068. https://doi.org/10.1002/2013GL058109

Prieto, G. A., Froment, B., Yu, C., Poli, P., & Abercrombie, R. (2017). Earthquake rupture below the brittle-ductile transition in continental lithospheric mantle. *Science Advances*, *3*(3), e1602642.

Ruiz, S, & Madariaga, R (2013). Kinematic and dynamic inversion of the 2008 northern Iwate earthquake. *Bulletin of the Seismological Society of America*, *103*(2A), 694–708.

Scholz, C. H. (1998). Earthquakes and friction laws. *Nature*, *391*(6662), 37.

Singh, S. K., & Ordaz, M. (1994). Seismic energy release in Mexican subduction zone earthquakes. *Bulletin of the Seismological Society of America*, *84*, 1533–1550.

Singh, S. K., Pérez-Campos, X., Espíndola, V., Cruz-Atienza, V., & Iglesias, A (2014). Intraslab earthquake of 16 June 2013 (M_w5.9), one of the closest such events to Mexico City. *Seismological Research Letters*, *85*(2), 268–277.

Singh, S. K., Reinoso, E., Arroyo, D., Ordaz, M., Cruz-Atienza, V. M., Pérez-Campos, X., et al. (2018). Deadly intraslab Mexico earthquake of 19 September 2017 (M_w7.1): Ground motion and damage pattern in Mexico City. *Seismological Research Letters*. *89*(6), 2193–2203. https://doi.org/10.1785/0220180159

Suárez, G., Santoyo, M. A., Hjorleifsdottir, V., Iglesias, A., Villafuerte, C., & Cruz-Atienza, V. M. (2019). Large scale lithospheric detachment of the downgoing Cocos plate: The 8 September 2017 earthquake (M_w8.2). *Earth and Planetary Science Letters*, *509*, 9–14.

Suganthan, P. N. (1999). Particle swarm optimiser with neighbourhood operator. In *IEEE Proceedings of the 1999 congress on evolutionary computation-cec99 (cat. no. 99th8406)* (Vol. *3*, pp. 1958–1962).

Takahashi, E., & Scarfe, C. M. (1985). Melting of peridotite to 14 GPa and the genesis of komatiite. *Nature*, *315*, 566–568.

Twardzik, C, Das, S, & Madariaga, R (2014). Inversion for the physical parameters that control the source dynamics of the 2004 Parkfield earthquake. *Journal of Geophysical Research: Solid Earth*, *119*, 7010–7027. https://doi.org/10.1002/2014JB011238

Vallée, M., & Duet, V. (2016). A new database of source time functions (STFs) extracted from the SCARDEC method. *Physics of the Earth and Planetary Interiors*, *257*, 149–157.

Venkataraman, A., & Kanamori, H. (2004). Observational constraints on the fracture energy of subduction zone earthquakes. *Journal of Geophysical Research*, *109*, B05302. https://doi.org/10.1029/2003JB002549

Ye, L. (2018). *Personal Communication*. USA. California Institute of Technology.